PHOTONICS Research

Moiré meta-device for flexibly controlled Bessel beam generation

GUOCUI WANG,[1,2] TIAN ZHOU,[1] JIANZHOU HUANG,[1] XINKE WANG,[2] BIN HU,[1,3] AND YAN ZHANG[2,4]

[1]Beijing Engineering Research Center for Mixed Reality and Advanced Display, School of Optics and Photonics, Beijing Institute of Technology, Beijing 100081, China
[2]Beijing Key Laboratory of Metamaterials and Devices, Key Laboratory of Terahertz Optoelectronics, Ministry of Education, Beijing Advanced Innovation Center for Imaging Theory and Technology, Department of Physics, Capital Normal University, Beijing 100048, China
[3]e-mail: hubin@bit.edu.cn
[4]e-mail: yzhang@cnu.edu.cn

High-order Bessel beams are of great interest for most stable long-range optical quantum communications due to their unique nondiffraction, self-healing, and orbital angular-momentum-carrying capabilities. Until now, meta-surfaces based on Bessel beam generators are mostly static and focused on generating zero-order Bessel beams. A moiré meta-device made of two cascaded metasurfaces is a simple, effective strategy to dynamically manipulate the wavefront of electromagnetic (EM) waves by mutual rotation between the two metasurfaces. Here, an all-dielectric moiré meta-device integrated with the functions of an axicon and a spiral phase plate to generate terahertz Bessel beams is designed. Not only the order, but also the nondiffraction length of the generated Bessel beam can be continuously tuned. As a proof of concept of the feasibility of the platform, the case of tuning order is experimentally demonstrated. The experimental results are in good agreement with the theoretical expectations. In addition, we also numerically proved that the nondiffraction length of the Bessel beam can be adjusted with the same approach. The moiré meta-device platform is powerful in dynamically manipulating the wavefront of EM waves and provides an effective strategy for continuously controlling the properties of the Bessel beam, which may find applications in optical communications, particle manipulation, and super-resolution imaging. © 2022 Chinese Laser Press

https://doi.org/10.1364/PRJ.475973

1. INTRODUCTION

Bessel beams, which are a set of solutions of the free space Helmholtz equation and were first suggested by Durnin in 1987 [1], have attracted intensive attention due to their unique nondiffractive [2] and superior self-healing capabilities [3]. Higher-order Bessel beams (HOBBs), which carry orbital angular momentum with transport information encoded [4,5], are in principle excellent tools for stable, long-range optical quantum communications and optical manipulation [6,7]. The typical device to generate Bessel beams is an axicon [8] or an annular aperture [2]. Furthermore, the generation of HOBBs requires a Laguerre–Gaussian mode beam to illuminate the axicon [9]. However, these traditional methods suffer from low efficiency, bulky size, and a complicated manufacturing procedure. The emergence of metasurface provides a new approach to realize ultrathin, compact Bessel beam generators. Metasurfaces are the 2D equivalent of metamaterials, which are constructed from subwavelength planar microstructures with carefully tailored geometrics [10–12]. Metasurfaces exhibit extraordinary capabilities to control electromagnetic (EM) waves. Numerous ultrathin devices such as lenses based on metasurfaces [13,14], complex light field generation [15], anomalous reflection of light [16,17], and metasurface holograms [18,19] have been developed.

Many Bessel beam generators based on metallic metasurfaces also have been proposed [20–25]. However, most are limited by low efficiency due to the high loss in metals. Although a few high-efficiency Bessel beam generators have been demonstrated [26–29], all these elements unfortunately lack tunability and mostly focus on the generation of zeroth-order Bessel beams. The tunable metasurfaces integrated with functional materials, controlled by thermal [30], electrical [31], optical [32], and chemical [33] trigger modes have been proposed. These active devices can overcome the limitations of static metasurfaces. For example, an electronically engineered reflective metasurface was designed to flexibly manipulate the nondiffraction region of Bessel beams in the gigahertz (GHz) band [34], in which a varactor diode is embedded in the gap between two strips in the metasurface. Nevertheless, the implementation

of this method faces a great challenge in the terahertz (THz) and higher frequencies range because active elements such as PIN diodes and varactors are difficult to integrate with the reduced unit cell structures for shortened wavelengths. Very recently, an emerging moiré metasurface cascaded by two metasurfaces with mutual movement offers an alternative approach to dynamically control the wavefront of EM waves, which can be operated in a very wide frequency band from microwave to visible light [35,36]. Compared to a commonly tunable metasurface integrated with active materials, the moiré metasurfaces offer advantages that include continuous control of the wavefront, a large tuning range, more stable property, and easier operation [37–39].

Here, a moiré meta-device integrated with the phase distributions of a spiral plate and an axicon to flexibly control the order and nondiffraction length of a Bessel beam is proposed. As a proof of concept, an all-dielectric moiré meta-device to actively control the order of Bessel beams is designed and fabricated. Experimental results demonstrate that the proposed moiré meta-device exhibits the ability to generate not only the zeroth-order but also order-variable HOBBs without using additional vortex phase elements. The order of the HOBBs can be changed continuously by rotating one metasurface relative to the other. In addition, it is also numerically proven that the nondiffraction length of a Bessel beam can be continuously modulated by designing a moiré meta-device.

2. PRINCIPLE AND DESIGN METHOD

The schematic diagram of the designed moiré meta-device to generate and manipulate Bessel beams is illustrated in Fig. 1. A pair of planar all dielectric metasurfaces with different predesigned phase distributions and placed face to face was used to construct the moiré meta-device. The terahertz (THz) Bessel beams can be generated after a plane THz beam passes through the cascaded metasurfaces. Both the order and the nondiffraction length of the Bessel beams can be adjusted flexibly by the mutual rotation of the two metasurfaces.
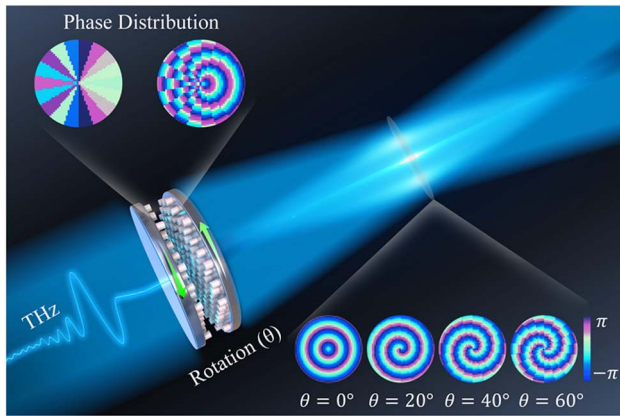

Fig. 1. Schematic of the proposed moiré meta-device for order-variable Bessel beams generation. The moiré meta-device is cascaded by two metasurfaces with different phase profiles. Bessel beams can be obtained after a THz beam passes through the moiré meta-device. The order of the Bessel beam can be changed by mutual rotating with a step of 20° between the two metasurfaces.

The basic principle used to construct a moiré meta-device is described in this way. Suppose two components $\Phi_1(r, \alpha)$ and $\Phi_2(r, \alpha)$ to express the phase profiles of the two metasurfaces, respectively, where r and α are the coordinate parameters in the polar coordinates. If a metasurface has a shift in one of the coordinates, for example, metasurface 1 has a shift of α_1 and metasurface 2 has a shift of α_2 along the α axis, the joint phase after two cascading metasurfaces has the form [40]

$$\Phi_{\text{joint}} = \Phi_1(r, \alpha - \alpha_1) + \Phi_2(r, \alpha - \alpha_2)$$
$$= A(\alpha_1, \alpha_2)\Phi(r, \alpha) + B(\alpha_1, \alpha_2), \quad (1)$$

where $\Phi(r, \alpha)$ is the phase profile of the functional device to be realized; $A(\alpha_1, \alpha_2)$ and $B(\alpha_1, \alpha_2)$ are the variable scaling factors only dependent on the shifts of α_1 and α_2. Since $A(\alpha_1, \alpha_2)$ and $B(\alpha_1, \alpha_2)$ can be continuously adjusted by moving one metasurface relative to another, the phase of the whole device can be continuously tuned. Therefore, only $\Phi_1(r, \alpha)$ and $\Phi_2(r, \alpha)$ are required to design the tunable device. Here, we illustrate how to construct the phase profiles $\Phi_1(r, \alpha)$ and $\Phi_2(r, \alpha)$ for a tunable functional device.

The field distribution of a Bessel beam propagating along the z axis in the cylindrical coordinates (r, α, z) can be written as [29]

$$E(r, \alpha, z) = E_0 \exp(ik_z z) J_n(k_r r) \exp(il\alpha), \quad (2)$$

where E_0 is the amplitude, J_n is an nth-order Bessel function, k_z and k_r are the corresponding longitude and radial wavevectors, respectively, and l is the topological charge of the optical vortex, that is, the order of the HOBB. The conventional device to generate the HOBB requires the combination of a spiral plate and an axicon. To obtain the corresponding phase profile of the metasurface, the combination of a flat spiral phase plate and a flat axicon is required [20], as shown in Fig. 2(a). The phase profile of such an assembly in the polar coordinates is given as

$$\Phi(r, \alpha) = l\alpha + \frac{2\pi}{\lambda} r \sin\beta, \quad (3)$$

where $l\alpha$ corresponds to the wavefront of a flat spiral, l is the order of HOBB, $2\pi/\lambda r \sin\beta$ is the wavefront of a flat axicon, and $2\pi/\lambda$ is the wave vector in free space. β is the base angle of the flat axicon, which determines the nondiffraction length $D_Z = D/2 \tan\beta$ of the Bessel beam, and D is the diameter of the HOBB generator that is fixed for a fabricated device. Equation (3) suggests that the order or the nondiffraction length of the Bessel beam can be actively manipulated by controlling the factor l or β, respectively. Therefore, we suppose that the phase profiles of the two metasurfaces are

$$\Phi_1(r, \alpha) = \Phi_{11}(\alpha) + \Phi_{12}(r), \quad (4)$$

$$\Phi_2(r, \alpha) = \Phi_{21}(\alpha) + \Phi_{22}(r), \quad (5)$$

where $\Phi_{11}(\alpha)$ and $\Phi_{21}(\alpha)$ represent the phase profiles only dependent on α, while $\Phi_{12}(r)$ and $\Phi_{22}(r)$ represent the phase profiles only dependent on r. Constructing $\Phi_1(r, \alpha)$ and $\Phi_2(r, \alpha)$ with different expressions, a Bessel beam generator can be obtained. With this generator, the properties of Bessel beams, not only the order but also the nondiffraction length, can be dynamically manipulated. For example, if we
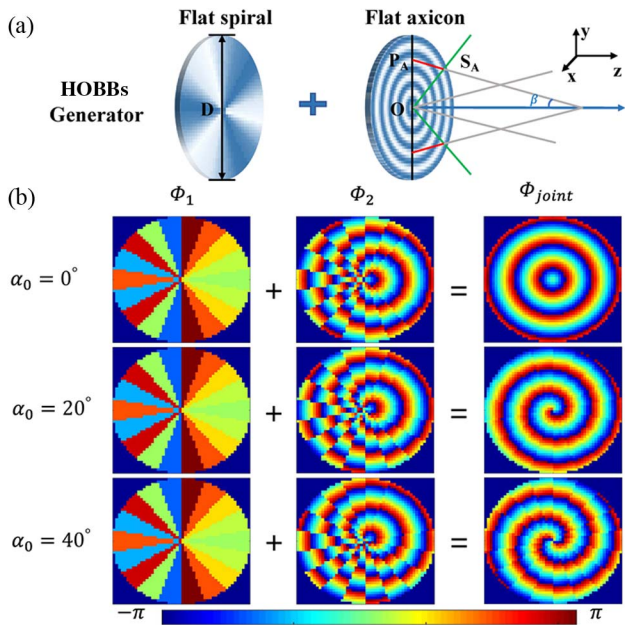
Fig. 2. Design principle of the proposed moiré meta-device to generate order-variable Bessel beams. (a) Schematic of the combination of a flat spiral and a flat axicon. (b) Design principle of the proposed moiré meta-device to generate order-variable Bessel beams. Φ_1 and Φ_2 are the phase profiles of metasurface 1 and metasurface 2, respectively. Φ_{joint} is the phase profile of the functional device to be realized. α_0 is the mutual rotation angle between two metasurfaces.

assume that $\Phi_{11}(\alpha) = \alpha^2$, $\Phi_{12}(r) = 0$, $\Phi_{21}(\alpha) = -\alpha^2$, $\Phi_{22}(r) = 2\pi/\lambda r \sin\beta$, $\alpha_1 = 0$, and $\alpha_2 = \alpha_0$, then Eq. (1) becomes

$$\Phi_{\mathrm{joint}} = 2\alpha_0 \alpha + \frac{2\pi}{\lambda} r \sin\beta + \alpha_0^2. \qquad (6)$$

Compared to Eq. (3), it can be found that the order number is $l = 2\alpha_0$, and α_0^2 is a constant phase offset. As such, the order number can be easily tuned by adjusting the mutual rotation α_0. Similarly, assuming that $\Phi_{11}(\alpha) = l\alpha$, $\Phi_{12}(r) = ar\alpha$, $\Phi_{21}(\alpha) = 0$, $\Phi_{22}(r) = -ar\alpha$, $\alpha_1 = 0$, and $\alpha_2 = \alpha_0$, then Eq. (1) becomes

$$\Phi_{\mathrm{joint}} = l\alpha + a\alpha_0 r, \qquad (7)$$

where a is a freely selectable constant. When Eq. (7) is compared to Eq. (3), it is found that the base angle is $\beta = \arcsin(\frac{a\lambda\alpha_0}{2\pi})$, indicating that the base angle of the flat axicon can be controlled by adjusting α_0; therefore, the nondiffraction length can be continuously adjusted. As such, a flexible manipulation of the Bessel beam can be achieved by the proposed moiré meta-device. Here, we experimentally demonstrate the control of the order. For the moiré meta-device, a sectoring effect is inevitable due to the 2π periodicity of rotation, which will affect the quality of the Bessel beams and reduce the efficiency of the device. Such issues can be overcome by phase quantization and compensation [41]. Then, the phase profile of metasurfaces can be expressed as (see detailed derivations in Appendix A)

$$\Phi_1 = \frac{m^2}{N} \pi, \qquad (8)$$

$$\Phi_2 = -\frac{m^2}{N} \pi + \frac{2\pi}{\lambda} r \sin\beta, \qquad (9)$$

where N is an even integer, expressed as $N = 2\pi/\Delta\alpha$, and m is an integer, expressed as $m = \mathrm{round}(\alpha/\Delta\alpha)$. Figure 2(b) illustrates the schematic of the phase profiles of the two metasurfaces and the joint phase distributions under different rotation angles. The Bessel beams with higher orders can be obtained by increasing the mutual rotation angle α_0.

The design schematic diagram of the proposed moiré meta-device is shown in Fig. 3. The basic element constructing the metasurfaces is high-resistivity silicon ($n = 3.4$) cylindrical pillars with uniform height h and variable diameters d, which are prepared on the same silicon substrate with a height of H and period of P, as shown in Fig. 3(a). To achieve full-phase modulation of 2π at the target frequency of 0.6 THz, we performed full-wave numerical simulations using commercial software with the finite difference time domain (FDTD) method to sweep the parameters P, H, h, and d. The values of P, H, and h are optimized and determined to be 200 μm, 700 μm, and 300 μm, respectively. Under the x-polarized illumination, the transmission amplitude and phase shifts of the co-polarization components were abstracted. Figure 3(b) gives the dependence of the transmission amplitude and phase on the diameter d of the silicon pillar at the operation frequency. The amplitude is maintained around 0.75 and the phase increases from 0 to 2π as d increases from 30 to 180 μm. Then, the pillars with different diameters were arranged according to the predesigned phase modulation profiles to construct
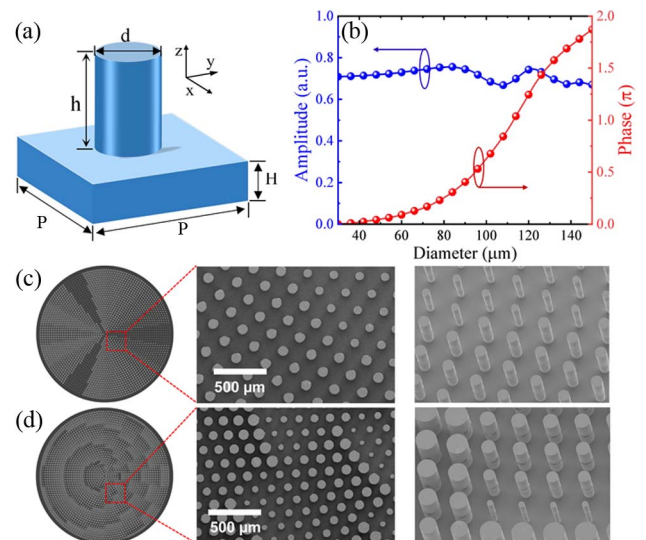

Fig. 3. Schematic of designed processes of the metasurfaces. (a) Basic elements of the metasurface are high-resistivity silicon pillars with a height h of 300 μm and variable diameters d ranging from 30 to 180 μm on a silicon substrate with a period P of 200 μm and height H of 700 μm. (b) Transmission and phase shift of silicon pillars with different diameters at the operation frequency of 0.6 THz. (c), (d) SEM images of fabricated metasurface 1 and metasurface 2, respectively. The scale bar is 200 μm.

corresponding metasurfaces. To verify the feasibility of the devices in the experiment, a moiré meta-device with a diameter of 12 mm was fabricated using standard ultraviolet lithography and inductively coupled plasma (ICP) etching technology. Details of the sample fabrication can be found in Appendix B. Figures 3(c) and 3(d) illustrate the structure arrangements and SEM images of a part of the fabricated metasurface 1 and metasurface 2, respectively.

3. RESULTS AND DISCUSSION

A THz focal-plane imaging system shown in Fig. 4(a) is used to characterize the function of the proposed device. The details about the system can be found in Appendix B. To verify the function validity of the proposed moiré meta-device as a Bessel beam generator, we measured the transmitted field distribution of the moiré meta-device with a mutual rotation of 0° in serial image planes by moving the sample along the z direction with a 28 mm scan range and a 0.5 mm scan step, and then mapped the longitudinal cross-section of the transmitted field. The position of the sample closest to the probe crystal was set as $z = 0$, and the center of the beam spot in each x–y plane was set as the origin. It should be mentioned that the alignment between the two metasurfaces can significantly affect the performance of the moiré meta-device. Thus, a mask method for the alignment is designed in our experiment (see Appendix B). Figure 4(b1) illustrates the longitudinal amplitude profile of the generated optical field along the propagation direction at the

operating frequency of 0.6 THz, whereas Fig. 4(b2) gives the transverse amplitude profile at $z = 11$ mm. The longitudinal amplitude shows a propagation invariance in the process of propagation and the transverse amplitude profile presents an axially symmetric circular central peak as well as two concentric ring side lobes. In addition, the corresponding longitudinal (on the y–z plane) and transverse (on the x–y plane) phase profiles are shown in Figs. 4(b3) and 4(b4), respectively. On the y–z plane, the longitudinal phase distribution manifests the interference effect of the THz beams and the phase always keeps a flat plane around the optical axis in the diffraction-free region, which suggests that the THz field consistently maintains the constructive interference at different propagation distances. This is the reason causing the nondiffractive feature of the Bessel beam. On the x–y plane, the transverse phase distribution presents several concentric circles, and the phase value almost keeps constant in each circular region. Besides, a phase jump of π occurs on the interface between the adjacent circles. The features described above are consistent with the typical properties of a zeroth-order Bessel beam [42]; that is, the zeroth-order Bessel beam was generated by the proposed moiré meta-device when the mutual rotation between two metasurfaces is 0°. These are also observed in corresponding simulation results shown in Figs. 4(c1)–4(c4). Detailed simulation execution can be found in Appendix B. It is noted that the experimental results are in good agreement with the simulation results. To more intuitively compare the properties of the Bessel beam obtained in the experiment and simulation, profiles along the horizontal cut lines across the centers of Figs. 4(b1)–4(b4) and 4(c1)–4(c4) are extracted and plotted together. The nondiffraction range D_Z is defined as the FWHM of the amplitude profile along the propagation direction [42]. As shown in Fig. 4(d1), the D_Z of the Bessel beam along the propagation direction is evaluated as 10.5 mm in experiment, and 15.5 mm in the simulation. The FWHM of the transverse field illustrated in Fig. 4(d2) is 0.83 mm in the experiment, and 0.80 mm in the simulation. The phase variation is almost linear in the nondiffractive region, as shown in Fig. 4(d3), and the transverse phase jumps periodically between 0 and π in the experiment and simulation, as shown in Fig. 4(d4). As such, the moiré meta-device can generate a Bessel beam quite well, and the experimental results agree well with the simulation results, except for a slight deviation in the FWHM along the propagation direction due to the fabricating error, misalignment, and inherent errors in the system.

Usually, by adding a spiral phase to the axicon phase, an HOBB will be formed. In addition, the order of Bessel beam could be changed by using a spiral phase with different helical orders. In our experiment, the helical orders of the spiral phase can be flexibly controlled by mutually rotating two metasurfaces with different angles in the proposed moiré meta-device. To assess the capacity of our moiré meta-device in changing the order of the Bessel beams, the transmitted fields of the moiré meta-device under different mutual rotations between two metasurfaces of 0°, 20°, 40°, 60°, and 80° were measured. Both amplitudes and phase profiles in simulations and experiments were obtained at 0.6 THz and the results are displayed in Fig. 5. When the mutual rotation angle equals 0°, the
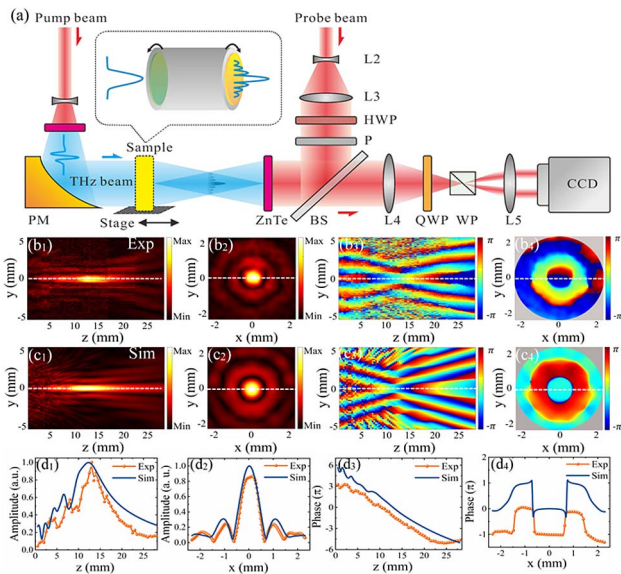

Fig. 4. Experimental results. (a) Schematic of experimental setup. PM, parabolic mirror; HWP, half-wave plate; P, polarizer; BS, beam splitter; QWP, quarter-wave plate; WP, Wollaston prism; and CCD, charge-coupled device. (b) Experimental and (c) simulated results for the zeroth-order Bessel beam when the mutual rotation of two metasurfaces is 0°. Two columns on the left are the normalized amplitudes on the y–z plane and the x–y plane, and on the right on the y–z plane and the x–y plane are the corresponding phase profiles. (d) Transverse amplitude and phase profiles along the horizontal white dotted cut lines across the centers of experiment and simulation results.

Research Article

amplitude distribution shown in Fig. 5(a1) presents an axially symmetric circular central peak as well as two concentric ring side lobes, whereas the phase profile shown in Fig. 5(b1) is also a concentric ring with a phase jump of π, which means that a zeroth-order Bessel beam is generated. The circular central peak in the amplitude distribution was transformed into the doughnut shape with a central dark core and an annular side lobe when the mutual rotation was changed. The size of central dark core was gradually increased when the mutual rotation varied from 20° to 80° with a step of 20°, as shown in Figs. 5(a2)–5(a5). Going around the circle, the phase presents spiral modalities with multiple 2π periods, and the periodicity increased from 1 to 4, as shown in Figs. 5(b2)–5(b5). This means that the HOBBs are generated by the proposed moiré meta-device and the orders of the Bessel beam were changed linearly from 0 to 4 by rotating one metasurface relative to another metasurface. Figures 5(c) and 5(d) give the simulation amplitude and phase profile, respectively. Good agreement with experimental data is found. This example demonstrates the power of the proposed moiré meta-device in active control of the Bessel beam generation.

Usually, the nondiffraction length of a Bessel beam can be adjusted by changing the base angle of an axicon. As shown in Eq. (7), using our designed moiré meta-device we can flexibly control the base angle of a flat axicon by mutually rotating two metasurfaces with different angles. This means that nondiffraction length of the Bessel beam can be flexibly controlled by the proposed moiré meta-device. To demonstrate the ability of this flexible control, we designed another moiré meta-device that consisted of two other metasurfaces with different phase profiles and simulated the transmission field distribution of the moiré meta-device along the direction of propagation in the Fresnel region. According to Eqs. (4), (5), and (7), the phase profiles of two metasurfaces, $\Phi_1(r, \alpha)$ and $\Phi_2(r, \alpha)$, can be obtained by setting $\Phi_{11}(\alpha) = l\alpha$, $\Phi_{12}(r) = ar\alpha$, $\Phi_{21}(\alpha) = 0$,

and $\Phi_{22}(r) = -ar\alpha$. Again, the undesired sectoring effect exists in the joint phase of the devices. Such a sector can be avoided by adopting a rounding operation [35], and the phase profiles of two metasurfaces can be written as

$$\Phi_1 = l\alpha + \text{round}(ar)\alpha, \tag{10}$$

$$\Phi_2 = -\text{round}(ar)\alpha. \tag{11}$$

For the convenience of quantitative characterization, the orbital angular momentum is set as $l = 0$, and the nondiffraction regions of zeroth-order Bessel beams under different mutual rotation angles are characterized. Figure 6(a) illustrates the phase distribution of the entire 12 mm diameter cascaded metasurfaces on the plane that is 1 mm away from the device under different mutual rotation angles obtained using the FDTD solver, and the field distribution of Bessel beam on the $y–z$ plane performed at 0.6 THz. It can be clearly observed that the length of the nondiffraction region decreases as the angle increases. To quantitatively characterize the change of the nondiffraction length with the mutual rotation angle, the cut lines across the centers of the field distribution of the Bessel beam on the $y–z$ plane are extracted and plotted together, as shown in Fig. 6(b). By calculating the FWHM of the lines in Fig. 6(b), the lengths of the nondiffracting region are calculated as $D_Z = 74$, 22, 12, and 10 mm, respectively. In addition, the

Fig. 6. Simulated results for nondiffraction region variable Bessel beam generation based on the moiré meta-device with the mutual rotation of two metasurfaces changing from 15° to 60° with a step of 15°. (a) Near-field phase distribution of entire 12 mm diameter cascaded metasurfaces on the plane that is 1 mm away from the device obtained using the FDTD solver and field distribution of the device along the direction of propagation on the $y–z$ plane. (b) Cut lines across the centers of field distribution illustrated in (a).
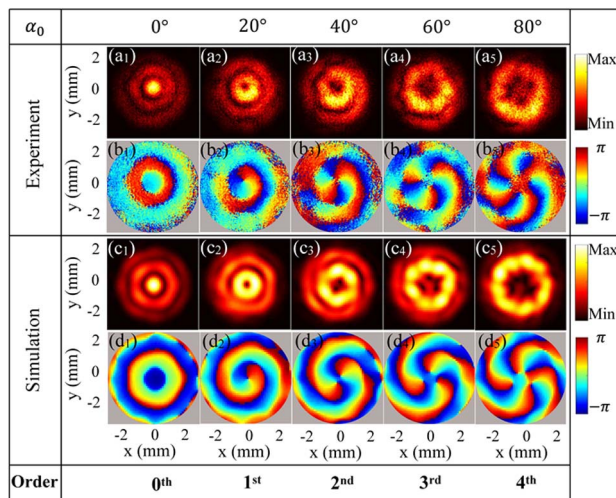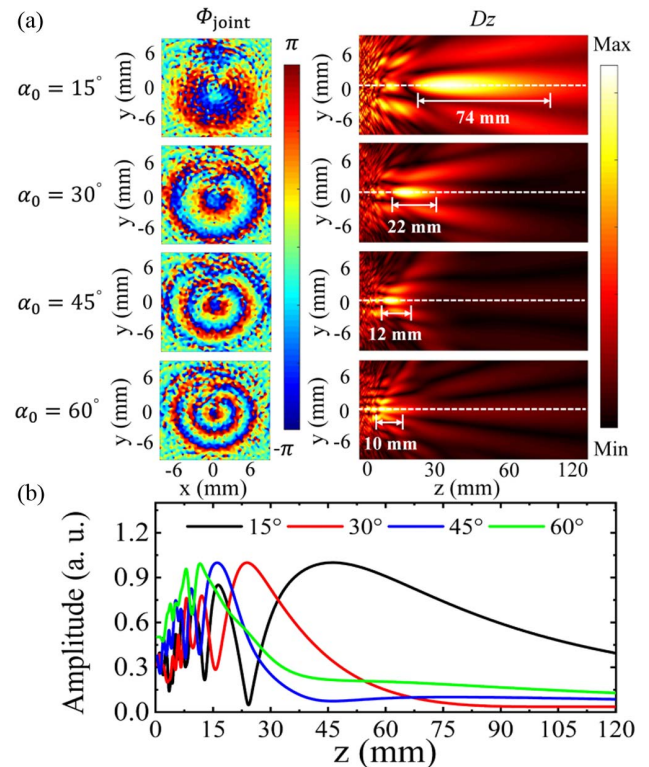
Fig. 5. Experimental and simulated results for order-variable Bessel beam generation based on the moiré meta-device with the mutual rotation of two metasurfaces changing from 0° to 80° with a step of 20°. (a)–(b) Normalized amplitude and phase profiles measured in the experiment. (c)–(d) Normalized amplitude and phase profiles obtained in the simulation.

length of the nondiffraction region for high-order Bessel beams such as first-order and second-order beams is also simulated (see Appendix C).

4. CONCLUSION

In summary, we have proposed a platform for a moiré meta-device that can dynamically manipulate the wavefront of EM waves without additional active elements. Based on this platform, both the order and nondiffraction range of the Bessel beam can be actively controlled. An all-dielectric moiré meta-device to generate order-variable Bessel beams was designed and experimentally demonstrated. By a simple mutual rotation of two cascading metasurfaces, the order of the Bessel beam can be continuously changed. The experimental results are in good agreement with the simulations. In addition, the numerical results proved that the length of the nondiffraction region in the Bessel beam can also be flexibly controlled by the designed moiré meta-device. We believe this moiré meta-device platform provides a simple, effective strategy to flexibly manipulate the properties of a Bessel beam, both the order and nondiffraction region, which could find applications in stable, long-range optical quantum communications, particle manipulation, and high-resolution imaging.

APPENDIX A: DERIVATION OF PHASE AMBIGUITY CORRECTION

A sectoring effect caused by the 2π ambiguity of rotation is inevitable in the moiré meta-device because part of the region shifted out of the defined region $[0, 2\pi]$ when the metasurface is rotated, and the overall emergent phase profile is split into two sectors. For example, the phase profiles of two metasurfaces used to control the order of the Bessel beams are given as

$$\Phi_1(r, \alpha) = \alpha^2, \tag{A1}$$

$$\Phi_2(r, \alpha) = -\alpha^2 + \frac{2\pi}{\lambda} r \sin \beta. \tag{A2}$$

After a rotation of α_0, the phase function in Eqs. (A1) and (A2) becomes

$$\Phi_1(r, \alpha) = \alpha^2, \tag{A3}$$

$$\Phi_2(r, \alpha) = \begin{cases} -[\alpha - (\alpha - 2\pi)]^2 + \frac{2\pi}{\lambda} r \sin \beta, & 0 < \alpha \leq \alpha_0 \\ -(\alpha - \alpha_0) + \frac{2\pi}{\lambda} r \sin \beta, & \alpha_0 < \alpha \leq 2\pi \end{cases}. \tag{A4}$$

Thus, the joint phase of the moiré meta-device can be written as

$$\Phi_{\text{joint}}(r, \alpha)$$
$$= \begin{cases} (2\alpha_0 - 4\pi)\alpha - \alpha_0 + 4\pi\alpha_0^2 - 4\pi^2 + \frac{2\pi}{\lambda} r \sin \beta, & 0 < \alpha \leq \alpha_0 \\ 2\alpha_0\alpha - \alpha_0^2 + \frac{2\pi}{\lambda} r \sin \beta, & \alpha_0 < \alpha \leq 2\pi \end{cases}. \tag{A5}$$

Compared to Eq. (3) in the main text, the order of the Bessel beams is

$$l = \begin{cases} 2\alpha_0 - 4\pi, & 0 < \alpha \leq \alpha_0 \\ 2\alpha_0, & \alpha_0 < \alpha \leq 2\pi \end{cases}. \tag{A6}$$

This suggests that two sectors yield two orders: one is $l = 2\alpha_0 - 4\pi$, and the other is $l = 2\alpha_0$, and the first one is an undesired sector. Therefore, the light is diffracted to rings with different radii, and the far-field intensity distribution is an open ring that will reduce the efficiency of the device. This problem can be overcome by a special quantization and offset of the phase [41]; thereby, the efficiency of the device can be improved. First, the angle range $[0, 2\pi]$ is divided into N (an even integer) small sectors by a step of $\Delta\alpha$, $N = 2\pi/\Delta\alpha$. Then, the phase profiles of two metasurfaces are quantified by the step of $\Delta\alpha$, and the ambiguous sector can be corrected by a phase compensation of integer multiples of 2π. After the quantification, the phase functions of two metasurfaces are expressed as

$$\Phi_1(r, m) = m^2 \frac{\pi}{N}, \tag{A7}$$

$$\Phi_2(r, m) = -m^2 \frac{\pi}{N} + \frac{2\pi}{\lambda} r \sin \beta, \tag{A8}$$

where m is an integer and described as

$$m = \text{round}(\alpha/\Delta\alpha_0). \tag{A9}$$

In addition, to obtain an integer number of the order, the rotation angle of α_0 should be an integer multiple of $\Delta\alpha$, which is given by

$$\alpha_0 = n\Delta\alpha, \tag{A10}$$

where n is an integer number and satisfies $-N \leq n \leq N$.

Considering the rotation angle of α_0, the total phase of the device is

$$\Phi_{\text{joint}} = \begin{cases} \frac{\pi}{N}\left[\text{round}\left(\frac{\alpha}{\Delta\alpha}\right)\right]^2 - \frac{\pi}{N}\left[\text{round}\left(\frac{\alpha(\alpha_0 - 2\pi)}{\Delta\alpha}\right)\right]^2 \\ + \frac{2\pi}{\lambda} r \sin \beta, \qquad 0 < \alpha \leq \alpha_0 \\ \frac{\pi}{N}\left[\text{round}\left(\frac{\alpha}{\Delta\alpha}\right)\right]^2 - \frac{\pi}{N}\left[\text{round}\left(\frac{\alpha - \alpha_0}{\Delta\alpha}\right)\right]^2 \\ + \frac{2\pi}{\lambda} r \sin \beta, \qquad \alpha_0 < \alpha \leq 2\pi \end{cases}. \tag{A11}$$

For the ambiguous sector $0 < \alpha \leq \alpha_0$, the corresponding total phase of the device can be transformed into

$$\Phi_{\text{joint}} = \frac{\pi}{N}\left[\text{round}\left(\frac{\alpha}{\Delta\alpha}\right)\right]^2 - \frac{\pi}{N}\left[\text{round}\left(\frac{\alpha - \alpha_0}{\Delta\alpha}\right) + N\right]^2$$
$$+ \frac{2\pi}{\lambda} r \sin \beta$$
$$= \frac{\pi}{N}\left[\text{round}\left(\frac{\alpha}{\Delta\alpha}\right)\right]^2 - \frac{\pi}{N}\left[\text{round}\left(\frac{\alpha - \alpha_0}{\Delta\alpha}\right)\right]^2$$
$$- 2\pi\text{round}\left(\frac{\alpha - \alpha_0}{\Delta\alpha}\right) + N\pi + \frac{2\pi}{\lambda} r \sin \beta$$
$$= \frac{\pi}{N}\left[\text{round}\left(\frac{\alpha}{\Delta\alpha}\right)\right]^2 - \frac{\pi}{N}\left[\text{round}\left(\frac{\alpha - \alpha_0}{\Delta\alpha}\right)\right]^2$$
$$- 2k\pi + \frac{2\pi}{\lambda} r \sin \beta$$
$$= \frac{\pi}{N}\left[\text{round}\left(\frac{\alpha}{\Delta\alpha}\right)\right]^2 - \frac{\pi}{N}\left[\text{round}\left(\frac{\alpha - \alpha_0}{\Delta\alpha}\right)\right]^2$$
$$+ \frac{2\pi}{\lambda} r \sin \beta. \tag{A12}$$

Obviously, the phase distributions of the sector $0 < \alpha \le \alpha_0$ and the sector $\alpha_0 < \alpha \le 2\pi$ are equivalent. Thus, the sectoring effect caused by the 2π ambiguity of rotation can be successfully eliminated. Thus, the phase profile of the device can be written as

$$
\begin{aligned}
\Phi_{\text{joint}} &= \frac{\pi}{N}\left[\text{round}\left(\frac{\alpha}{\Delta\alpha}\right)\right]^2 - \frac{\pi}{N}\left[\text{round}\left(\frac{\alpha - \alpha_0}{\Delta\alpha}\right)\right]^2 \\
&\quad + \frac{2\pi}{\lambda} r \sin\beta \\
&= \frac{\pi}{N}\left[\text{round}\left(\frac{\alpha}{\Delta\alpha}\right)\right]^2 - \frac{\pi}{N}\left[\text{round}\left(\frac{\alpha}{\Delta\alpha} - n\right)\right]^2 \\
&\quad + \frac{2\pi}{\lambda} r \sin\beta \\
&= \frac{\pi}{N}\left[\text{round}\left(\frac{\alpha}{\Delta\alpha}\right)\right]^2 - \frac{\pi}{N}\left[\text{round}\left(\frac{\alpha}{\Delta\alpha}\right)\right]^2 \\
&\quad - 2\frac{\pi}{N} n\,\text{round}\left(\frac{\alpha}{\Delta\alpha}\right) - \frac{\pi}{N} n^2 + \frac{2\pi}{\lambda} r \sin\beta \\
&= 2\frac{\pi}{N} n\,\text{round}\left(\frac{\alpha}{\Delta\alpha}\right) - n^2\frac{\pi}{N} + \frac{2\pi}{\lambda} r \sin\beta \\
&= 2mn - n^2\frac{\pi}{N} + \frac{2\pi}{\lambda} r \sin\beta.
\end{aligned}
\tag{A13}
$$

Comparing Eq. (A13) with Eq. (A5), the target order of the Bessel beam obtained by the device is $l = n$.

APPENDIX B: SIMULATION AND EXPERIMENTAL SECTION

For the simulation of the cascaded metasurfaces, we obtained the complex amplitude distribution of the entire 12 mm diameter cascaded metasurfaces on the plane, which is 1 mm away from the device using the FDTD solver, where the distance between two metasurfaces is selected as 1 mm. Then, we calculated the field distribution in Fresnel region of the near-field complex amplitude using the Fresnel integral diffraction algorithm.

Standard ultraviolet lithography and inductively coupled plasma (ICP) etching technology were used to fabricate the samples. First, a high-resistivity silicon wafer ($\langle 100 \rangle$, 2000 Ω) that was 1000 μm thick with a diameter of 4 inches was cleaned in an ultrasonic bath. Then, a positive photoresist (AZP4620) film was put onto the silicon wafer by spin-coating and then baking. An aligned mask was used for the exposure of the photoresist film. After the development process, the image on the mask was transferred to the photoresist film. Next, the silicon wafer was etched using ICP etching with SF6 etch gas. Finally, the silicon pillars were obtained after the remaining photoresist was removed with acetone, and the wafer was cleaned and dried.

A THz focal-plane imaging system [43] was used to perform characterization of the sample. The 35 fs ultrashort laser pulses with an 800 nm central wavelength, 1 kHz repetition rate, and 900 mW average power started from a Ti:sapphire regenerator amplifier was split into two beams that were then used as the pump and probe beams to generate and detect THz waves. A 1 mm thick $\langle 100 \rangle$ ZnTe crystal was used to generate THz
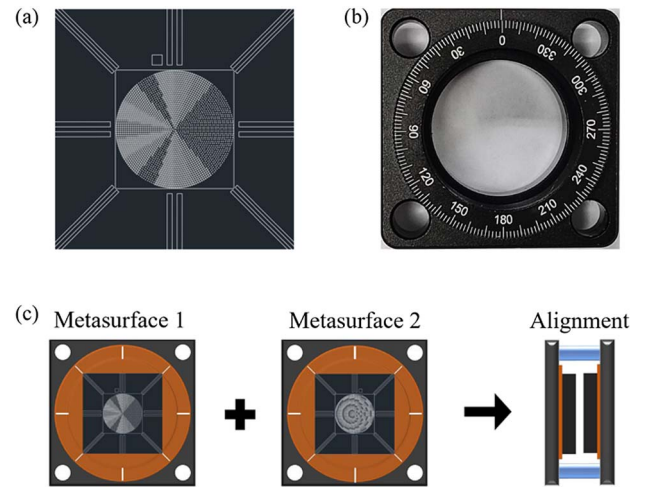

Fig. 7. Diagram of alignment method for two metasurfaces.

waves through the optical rectification effect, whereas another $\langle 100 \rangle$ ZnTe crystal (2 mm thick) was used to detect the THz waves using the Pockels effect. The polarization of the THz was controlled by a half-wave plate and a polarizer. Based on the balanced electro-optic detection technique, the temporal field distributions of a THz wave were captured using an imaging module consisting of two lenses, a Wollaston prism, a quarter-wave plate, and a CCD camera. Then, the amplitude and phase information of each frequency can be obtained through the Fourier transform operation of the temporal signal of each pixel.

A key point of the moiré meta-device is the alignment of two metasurfaces. Although the device will not lose its intended function if the two metasurfaces are not aligned perfectly, the performance of device will be significantly affected. Thus, an alignment method is proposed in our experiment. As illustrated in Fig. 7, a two-line type mark for alignment is designed during the sample processing. The samples are installed in a rotating frame with angle marks, as shown in Fig. 7(b). The angle marks serve two purposes: one is for alignment between the sample and the frame because the marks on the frame can be located at two-line marks of the sample; the other is a counter to show the rotation angle between the two metasurfaces. The two frames installed with the samples are mounted on a coaxial holder. Thus, two metasurfaces can be aligned through the mask discussed above. Generally speaking, the selection of distance between two layers depends on the phase gradient of the previous one. A larger phase gradient requires a smaller distance. At the same time, to avoid the coupling caused by the two metasurfaces, we recommend the distance to be 1–3 times of wavelengths.

APPENDIX C: MANIPULATION OF NONDIFFRACTION REGION IN HIGHER-ORDER BESSEL BEAMS

To characterize the change in the nondiffraction region with the rotation angle in higher-order Bessel beams, we simulate the far-field diffraction of the higher-order Bessel beams where
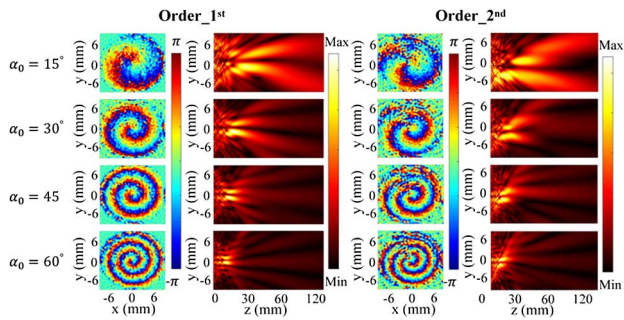
Fig. 8. Simulation results for nondiffraction region variable higher-order Bessel beams generation based on the moiré meta-device with the mutual rotation of two metasurfaces changing from 15° to 60° with a step of 15°.

the mutual rotation angles between two metasurface are equal to 15°, 30°, 45°, and 60°, respectively. Figure 8 shows the far-field diffraction of the first-order and second-order Bessel beams. It can be clearly seen that the length of nondiffraction region in both the first-order and second-order Bessel beams decreases as the rotation angle increases.

Disclosures. The authors declare no conflicts of interest.

Data Availability. Data underlying the results presented in this paper are not publicly available at this time but may be obtained from the authors upon reasonable request.

REFERENCES

1. J. Durnin, "Exact solution for nondiffracting beams. I. The scalar theory," J. Opt. Soc. Am. A **4**, 651–654 (1987).
2. J. Durnin, J. Miceli, and J. Eberlym, "Diffraction-free beams," Phys. Rev. Lett. **58**, 1499–1501 (1987).
3. Z. Bouchal, J. Wagner, and M. Chlup, "Self-reconstruction of a distorted nondiffracting beam," Opt. Commun. **151**, 207–211 (1998).
4. J. Wang, J. Yang, I. Fazal, N. Ahmed, Y. Yan, H. Huang, Y. Ren, Y. Yue, S. Dolinar, M. Tur, and A. Willner, "Terabit free-space data transmission employing orbital angular momentum multiplexing," Nat. Photonics **6**, 488–496 (2012).
5. N. Bozinovic, Y. Yue, Y. Ren, M. Tur, P. Kristensen, H. Huang, A. Willner, and S. Ramachandran, "Terabit-scale orbital angular momentum mode division multiplexing in fibers," Science **340**, 1545–1548 (2013).
6. K. Dholakia, P. Reece, and M. Gu, "Optical micromanipulation," Chem. Soc. Rev. **37**, 42–55 (2008).
7. M. McLaren, T. Mhlanga, M. Padgett, F. Roux, and A. Forbes, "Self-healing of quantum entanglement after an obstruction," Nat. Commun. **5**, 3248 (2014).
8. J. McLeod, "The axicon: a new type of optical element," J. Opt. Soc. Am. **44**, 592–597 (1954).
9. J. Arlt and K. Dholakia, "Generation of high-order Bessel beams by use of an axicon," Opt. Commun. **177**, 297–301 (2000).
10. N. Yu, P. Genevet, M. Kats, F. Aieta, J. Tetienne, F. Capasso, and Z. Gaburro, "Light propagation with phase discontinuities: generalized laws of reflection and refraction," Science **334**, 333–337 (2011).
11. S. Sun, Q. He, S. Xiao, Q. Xu, X. Li, and L. Zhou, "Gradient-index meta-surfaces as a bridge linking propagating waves and surface waves," Nat. Mater. **11**, 426–431 (2012).
12. L. Huang, X. Chen, H. Muhlenbernd, G. Li, B. Bai, Q. Tan, G. Jin, T. Zentgraf, and S. Zhang, "Dispersionless phase discontinuities for controlling light propagation," Nano Lett. **12**, 5705–5755 (2012).
13. S. Wang, P. Wu, V. Su, Y. Lai, C. Chu, J. Chen, S. Lu, J. Chen, B. Xu, C. Kuan, T. Li, S. Zhu, and D. Tsai, "Broadband achromatic optical metasurface devices," Nat. Commun. **8**, 187 (2017).
14. D. Hu, X. Wang, S. Feng, J. Ye, W. Sun, Q. Kan, P. Klar, and Y. Zhang, "Ultrathin terahertz planar elements," Adv. Opt. Mater. **1**, 186–191 (2013).
15. J. Guo, X. Wang, J. He, H. Zhao, S. Feng, P. Han, J. Ye, W. Sun, G. Situ, and Y. Zhang, "Generation of radial polarized Lorentz beam with single layer metasurface," Adv. Opt. Mater. **6**, 1700925 (2018).
16. Z. Li, E. Palacios, S. Butun, and K. Aydin, "Visible-frequency metasurfaces for broadband anomalous reflection and high-efficiency spectrum splitting," Nano Lett. **15**, 1615–1621 (2015).
17. Y. Li, J. Zhang, Y. Zhang, H. Chen, and Y. Fan, "Wideband, co-polarization anomalous reflection metasurface based on low-*Q* resonators," Appl. Phys. A **122**, 851 (2016).
18. D. Wen, F. Yue, G. Li, G. Zheng, K. Chan, S. Chen, M. Chen, K. Li, P. Wong, K. Cheah, E. Pun, S. Zhang, and X. Chen, "Helicity multiplexed broadband metasurface holograms," Nat. Commun. **6**, 8241 (2015).
19. G. Yoon, D. Lee, K. Nam, and J. Rho, "Pragmatic metasurface hologram at visible wavelength: the balance between diffraction efficiency and fabrication compatibility," ACS Photon. **5**, 1643–1647 (2018).
20. F. Aieta, P. Genevet, M. Kats, N. Yu, R. Blanchard, Z. Gahurro, and F. Capasso, "Aberration-free ultrathin flat lenses and axicons at telecom wavelengths based on plasmonic metasurfaces," Nano Lett. **12**, 4932–4936 (2012).
21. Y. Li, B. Cai, X. Wan, and T. Cui, "Diffraction-free surface waves by metasurfaces," Opt. Lett. **39**, 5888–5891 (2014).
22. X. Li, M. Pu, Z. Zhao, X. Ma, J. Jin, Y. Wang, P. Gao, and X. Luo, "Catenary nanostructures as compact Bessel beam generators," Sci. Rep. **6**, 20524 (2016).
23. Y. Shen, J. Yang, S. Kong, and S. Hu, "Integrated coding metasurface for multi-functional millimeter-wave manipulations," Opt. Lett. **44**, 2855–2858 (2019).
24. Z. Shen, M. Tang, P. Chen, S. Zhou, S. Ge, W. Duan, T. Wei, X. Liang, W. Hu, and Y. Lu, "Planar terahertz photonics mediated by liquid crystal polymers," Adv. Opt. Mater. **8**, 1902124 (2020).
25. J. Li, L. Zhang, M. Zhang, H. Su, I. Li, S. Ruan, and H. Liang, "Wearable conformal metasurfaces for polarization division multiplexing," Adv. Opt. Mater. **8**, 2000068 (2020).
26. C. Pfeiffer and A. Grbic, "Controlling vector Bessel beams with metasurfaces," Phys. Rev. Appl. **2**, 044012 (2014).
27. Z. Ma, S. Hanham, P. Albella, B. Ng, H. Lu, Y. Gong, S. Maier, and M. Hong, "Terahertz all-dielectric magnetic mirror metasurfaces," ACS Photon. **3**, 1010–1018 (2016).
28. W. Chen, M. Khorasaninejad, A. Zhu, J. Oh, R. Devlin, A. Zaidi, and F. Capasso, "Generation of wavelength-independent subwavelength Bessel beams using metasurfaces," Light Sci. Appl. **6**, e16259 (2017).
29. Z. Lin, X. Li, R. Zhao, X. Song, Y. Wang, and L. Huang, "High-efficiency Bessel beam array generation by Huygens metasurfaces," Nanophotonics **8**, 1079–1085 (2019).
30. F. Zhang, X. Xie, M. Pu, Y. Guo, X. Ma, X. Li, X. J. Luo, Q. He, H. Yu, and X. Luo, "Multistate switching of photonic angular momentum coupling in phase-change metadevices," Adv. Mater. **32**, 1908194 (2020).
31. W. Liu, B. Hu, Z. Huang, H. Guan, H. Li, X. Wang, Y. Zhang, H. Yin, X. Xiong, J. Liu, and Y. Wang, "Graphene-enabled electrically controlled terahertz meta-lens," Photon. Res. **6**, 703–708 (2018).
32. J. Guo, T. Wang, H. Zhao, X. Wang, S. Feng, P. , Han, W. Sun, J. Ye, G. Situ, and H. Chen, "Reconfigurable terahertz metasurface pure phase holograms," Adv. Opt. Mater. **7**, 1801696 (2019).

33. J. Li, S. Kamin, G. Zheng, F. Neubrech, S. Zhang, and N. Liu, "Addressable metasurfaces for dynamic holography and optical information encryption," Sci. Adv. **4**, eaar6768 (2018).

34. R. Feng, B. Ratni, J. Yi, Z. Jiang, H. Zhang, A. de Lustrac, and S. Burokur, "Flexible manipulation of Bessel-like beams with a reconfigurable metasurface," Adv. Opt. Mater. **8**, 2001084 (2020).

35. S. Bernet and M. Ritsch-Marte, "Adjustable refractive power from diffractive moiré elements," Appl. Opt. **47**, 3722–3730 (2008).

36. Y. Guo, M. Pu, X. Ma, X. Li, R. Shi, and X. Luo, "Experimental demonstration of a continuous varifocal metalens with large zoom range and high imaging resolution," Appl. Phys. Lett. **115**, 163103 (2019).

37. Y. Wei, Y. Wang, X. Feng, S. Xiao, Z. Wang, T. Hu, M. Hu, J. Song, M. Wegener, M. Zhao, J. Xia, and Z. Yang, "Compact optical polarization-insensitive zoom metalens doublet," Adv. Opt. Mater. **8**, 2000142 (2020).

38. Y. Luo, C. Chu, S. Vyas, H. Kuo, Y. Chia, M. Chen, Y. Huang, and D. Tsai, "Varifocal metalens for optical sectioning fluorescence microscopy," Nano Lett. **21**, 5133–5142 (2021).

39. C. Ogawa, S. Nakamura, T. Aso, S. Ikezawa, and K. Iwami, "Rotational varifocal moiré metalens made of single-crystal silicon meta-atoms for visible wavelengths," Nanophotonics **11**, 1941–1948 (2022).

40. Z. Du, B. Hu, W. Liu, and Y. Wang, "Tunable beam deflector by mutual motion of cascaded bilayer metasurface," J. Opt. **21**, 115101 (2019).

41. A. Grewe and S. Sinzinger, "Efficient quantization of tunable helix phase plates," Opt. Lett. **41**, 4755–4758 (2016).

42. Z. Wu, X. Wang, W. Sun, S. Feng, P. Han, J. Ye, and Y. Zhang, "Vector characterization of zero-order terahertz Bessel beams with linear and circular polarizations," Sci. Rep. **7**, 13929 (2017).

43. X. Wang, Y. Cui, W. Sun, J. Ye, and Y. Zhang, "Terahertz polarization real-time imaging based on balanced electro-optic detection," J. Opt. Soc. Am. A **27**, 2387–2393 (2010).